Int. J. Multiphase Flow Vol. 19, No. 2, pp. 281–294, 1993
Printed in Great Britain. All rights reserved

0301-9322/93 $6.00 + 0.00
Copyright © 1993 Pergamon Press Ltd

AN EXPERIMENTAL STUDY ON AIR CARRYUNDER DUE TO A PLUNGING LIQUID JET

F. BONETTO† and R. T. LAHEY JR
Rensselaer Polytechnic Institute, Troy, NY 12180-3590, U.S.A.

(Received 19 March 1992; in revised form 26 October 1992)

Abstract—This paper presents experimental data on the air entrainment process for a plunging liquid jet. Local data, including the size distribution of the bubble diameter, void fraction, bubble velocities and turbulent liquid velocities were obtained using a fiber optics phase Doppler anemometer system. A dual element conductivity probe was also used to measure the spatial distribution of the local void fraction. For the larger bubbles, the turbulence of the plunging jet was parametrically controlled using a specially designed nozzle and the turbulence intensity was measured using a laser Doppler anemometer system.

Key Words: plunging liquid jet, two-phase flow, air carryunder

INTRODUCTION

A good understanding of the air carryunder and bubble dispersion process associated with a plunging liquid jet is vital if one is to be able to quantify such diverse phenomena as sea surface chemistry, the meteorological significance of (breaking) ocean waves, the performance of certain type of chemical reactors, the "greenhouse" effect (i.e. the absorption of CO_2 by the oceans) and a number of other important maritime-related applications. The absorption of greenhouse gases into the ocean has been hypothesized to be highly dependent upon the air carryunder that occurs due to breaking waves. This process can be approximated with a plunging liquid jet (Monahan & Torgersen 1991; Kerman 1984). In particular, the air entrainment process due to the breaking bow waves of surface ships may cause long (i.e. up to 5 km in length) wakes. Naturally easily detectable wakes are undesirable for naval warships. In addition, the air carryunder that occurs at most hydraulic structures in rivers is primarily responsible for the large air/water mass transfer that is associated with these structures (Avery & Novak 1978). Also, air entrainment plays an important role in slug flow phenomena. The liquid film surrounding the Taylor bubble has a mean flow in the opposite direction from the Taylor bubble. This liquid forms a type of plunging jet that produces a surface depression in the rear part of the Taylor bubble. When the annular liquid jet exceeds a critical velocity, the plunging liquid jet entrains small bubbles from the air in the Taylor bubble. These bubbles follow the Taylor bubbles in the liquid slug.

A number of prior studies have been performed in which axisymmetric plunging jets have been used to investigate the air carryunder process. These include the works of Lin & Donnelly (1966), Burgess *et al.* (1972), Van De Sande & Smith (1973), Koga (1982), McKeogh & Ervine (1981), Detsch & Sharma (1990), Ohkawa *et al.* (1986), Ervine *et al.* (1980), McKeogh & Elsaway (1980), Ervine & Falvey (1987), Blanchard & Cipriano (1981) and Sene (1988).

Unfortunately, in most of these experiments only global measurements were made. While such measurements may allow one to correlate an onset-of-air-carryunder criteria, they provide very limited information on the fluid mechanics of bubble entrainment and the resultant dispersion process in the induced two-phase jet.

The primary objective of this research was to obtain detailed local data in the two-phase flow region of a plunging liquid jet. We have obtained the local (turbulent) velocity of the liquid, the velocity of the gas bubbles, the bubble size distribution for bubbles smaller than about 1.0 mm and the void fraction of the gas phase. The combined probability density function (pdf) of the bubble size and velocity has not been measured before. The pdf for bubble diameters is needed to compute the interfacial area density, an important parameter which helps determine the mass transfer

†Permanent address: Centro Atómico Bariloche, 8400 Bariloche RN, Argentina.

characteristics of the two-phase flow. Finally, the pdf of the bubble velocity is needed to estimate the total time that the bubbles remain submerged and therefore able to transfer mass.

EXPERIMENTAL SETUP

As shown in figure 1, a converging nozzle oriented vertically produced an axisymmetric liquid (i.e. water) jet. This jet impacted a pool of water at 90° and, when a threshold velocity was exceeded, it was observed that the plunging liquid jet caused air entrainment. In agreement with the observations of McKeogh & Ervine (1981), different two-phase jet characteristics were noted, depending on the turbulence intensity of the plunging liquid jet. For a laminar liquid jet (i.e. one having a turbulence intensity less than about 0.8%) the diameters of the induced bubbles were in the range 15–300 μm. On the other hand, for a liquid jet turbulence intensity of about 3%, the entrained bubbles had diameters in the range 1–3 mm. Our definition of a rough and smooth jet should be considered only as an easy way to refer to one particular turbulence intensity. In particular, rough means a turbulence intensity of about 3% while smooth means about 0.8%. Another candidate for the distinction was the Reynolds number (Re). However, this is not appropriate because after the contraction, with the same Re we may have different turbulence intensity. These different turbulence intensities generate qualitatively different two-phase flows.

Figure 1 shows a schematic of the test loop, a screw pump was used to force the water through the nozzle as well through a bypass. The pump had a speed controller which was used for the coarse control of the liquid flow rate through the nozzle. In the bypass a valve was used for the fine control of the liquid flow rate. In order to damp out any flow oscillations, an accumulator was placed on the discharge side of the pump.

The acrylic conical nozzle, shown schematically in figure 2, consisted of an arrangement of honeycombs and screens followed by a smooth contraction. In this way the turbulence level of the liquid jet could be varied parametrically. The exit diameter of the nozzle was 5.1 mm, and this produced a liquid jet of about the same diameter. The acrylic tank which contained the water pool had dimensions, $0.914 \times 0.916 \times 1.465 = 1.265\ \mathrm{m}^3$. The suction of the tank was put as far from the liquid jet impact point as possible in order to minimize the influence of this flow on the two-phase jet's flow.

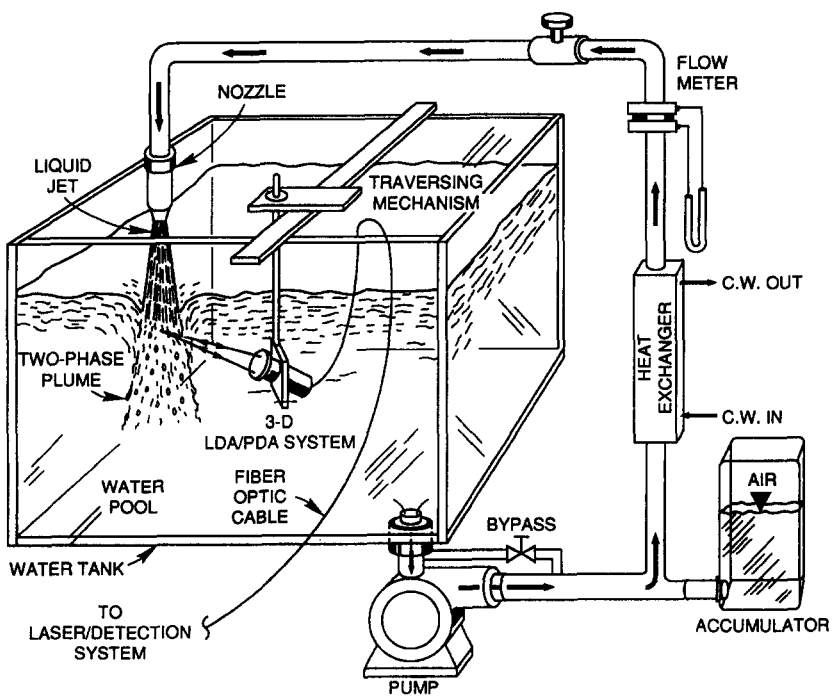

Figure 1. Schematic of the experimental apparatus.

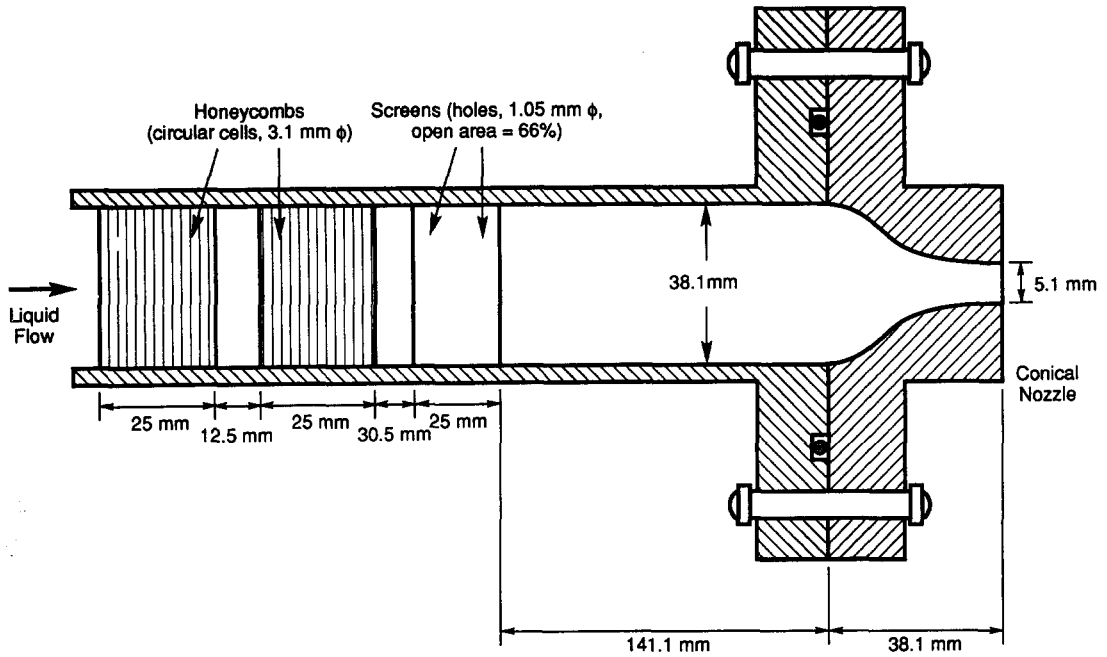

Figure 2. Schematic of the conical nozzle.

A DANTEC fiber-flow laser Doppler anemometer (LDA) system was used to nonintrusively measure the liquid and gas velocities (both the mean and fluctuations). This system consisted of submersible transmitting and receiving optics.

The transmitting optics were powered by a 10 W Ar-ion laser. The laser beam was split into two beams, where one beam passed through a Bragg cell to produce a fringe shift of 40 MHz in the measurement volume. Optical fiber wave guides conducted the laser beams to the submersible LDA heads. A 600 mm focal length lens was used in these experiments. A beam expander was also used to reduce the size of the measurement volume and increase the light intensity.

The receiving optics was used in a back-scattering configuration. Optical fibers conducted the scattered light to the photomultipliers after the light was optically filtered. The photomultipliers converted the optical signal into an electrical signal that was processed by a special covariance signal processor. An AT micro-computer collected and further processed the data.

The receiving optics used for the smooth jet employed a fiber phase Doppler anemometer (FPDA) system with 600 mm focal length lenses and a special aperture plate to maximize the bubble size range. The axial velocity of the liquid jet was used as the master signal for data collection. The collected light was transmitted through three optical fibers to a special FPDA device having three photodetectors for bubble size measurement.

The signals collected by the AT computer consisted of the:

—arrival time of the particles
—transit time of the particles
—velocity of the particles
—equivalent diameter of the particles.

Two different methods were used for the measurement of void fraction in the two-phase jet: a KfK impedance probe and the particle time fraction from the FPDA. The impedance probe consists of two electrically isolated electrodes; one at the tip of the probe and another downstream electrode which was always in contact with the liquid in the pool. The liquid (i.e. water) had a relatively high electrical conductivity and thus when the tip was in contact with the liquid a relatively high current flows through to a Wheatstone bridge circuit. The difference between the conductivities of the liquid and gas phases produces a different signal depending on whether there is liquid or gas present at the tip of the probe. The active element of the probe's tip was 150 μm in diameter and it was

calibrated with bubbles having diameters in the 1–3 mm range. This type of probe is a standard tool used for measuring local void fraction in air/water bubbly flows (Hewitt 1978).

The KfK impedance probe was used to measure the void fraction for the rough jet (which had bubbles of diameter in the range 1–3 mm) because the size of bubbles produced was out of the range of the FPDA (i.e. the air bubbles were too large for the lens size used). In contrast, for the measurement of void fraction when a smooth liquid jet was tested, the impedance probe could not be used because the size of the bubbles was the same order of magnitude as the size of the tip (i.e. the air bubbles were quite small). However, the FPDA could be, and was, used to measure the size distribution of the bubbles in this case.

A particle crossing the control volume of the LDA with a velocity u perpendicular to the LDA fringes produces light modulation in the photomultiplier that has a Doppler frequency of

$$f_D = \frac{2u}{\lambda} \sin\left(\frac{\theta}{2}\right), \qquad [1]$$

where

λ = wavelength of the laser light,
θ = angle between the laser beams
u = particle velocity component perpendicular to the fringes

and

f_D = Doppler frequency.

An important electromagnetic effect that is predicted by Mie's theory is that if a planar electromagnetic wave is reflected by a sphere of diameter d_p, the frequency of the reflected wave has the same frequency as the incident wave but it has a phase shift which depends on the sphere's diameter. In particular, a detector located at spherical coordinates (θ, ψ) will detect a phase difference, Θ, given by (Mie 1908):

$$\Theta = \pi \frac{d_p n}{\lambda} \sqrt{2}\left[\left(1 + \sin\frac{\theta}{2}\sin\phi\,\sin\psi - \cos\frac{\theta}{2}\cos\phi\right)^{1/2} - \left(1 - \sin\frac{\theta}{2}\sin\phi\,\sin\psi - \cos\frac{\theta}{2}\cos\phi\right)^{1/2}\right], \qquad [2]$$

where

n = index of refraction of the medium

and

d_p = particle diameter.

Thus, with two optical detectors we can evaluate the particle diameter by measuring the phase difference between the signals of the two detectors and the relative position of the detectors. Notice that the sensitivity of the system depends on the relative location of the detectors. The system used had three detectors, D1, D2 and D3. Detector D2 was near D1 (and thus had low sensitivity), and was configured for a dispersed particle size range of 0–800 μm. Detector D3 was far away from D1 (and thus had a high sensitivity) and it was used to increase the accuracy of the diameter measurement. That is, the phase difference between photomultipliers 1 and 2 was used to estimate the diameter subrange of the particles. The phase difference between photomultipliers 2 and 3 was then used to evaluate the diameter of the particle more accurately. The phase difference between photomultipliers 1 and 3 gave a consistency check (i.e. it was verified that the sum of the three phase differences was 2π). Durst & Eliasson (1975) were apparently the first to use this principle to measure the diameter of particles. Although Durst & Eliasson measured the diameter of relatively large particles (i.e. 2 mm in diameter) their method was extended to the μm range by Saffman *et al.* (1984).

The FPDA was calibrated using a suspension of polystyrene particles which had diameters of 9.5 ± 0.5 μm and a rotating steel ball of diameter 0.4 mm.

The LDA/FPDA system and the KfK impedance probe were mounted on a Benjamin Systems three-dimensional traversing mechanism having a 1 μm positioning resolution. The tip of the KfK

impedance probe was positioned 0.3 mm under the measurement volume of the LDA/FPDA system for void fraction measurements when a rough jet liquid was tested.

The turbulence intensity of the liquid jet at the nozzle exit was found to be one of the most important parameters affecting jet roughness and the size of the bubbles entrained by the plunging liquid jet. An arrangement of honeycombs and screens were used to control the turbulence intensity of the flow entering the conical nozzle. The attenuation of the turbulence due to the screens and honeycombs is given by

$$\left.\begin{aligned} f &= \frac{1}{1+K} && \text{axial reduction (Prandtl 1933)} \\ f &= \frac{1}{(1+K)^{1/2}} && \text{lateral reduction (Dryden \& Schuabauen 1947),} \end{aligned}\right\} \qquad [3]$$

where K is the pressure loss coefficient (in velocity heads).

Downstream of the honeycombs and screens the liquid flowed through an axisymmetric contraction. Prandtl (1933) showed that the attenuation of the turbulence in a convergent nozzle is:

$$\left.\begin{aligned} f &= 1/C^2 && \text{axial reduction} \\ f &= 1/C^{1/2} && \text{lateral reduction,} \end{aligned}\right\} \qquad [4]$$

where C is the area contraction ratio.

It was found that [3] and [4] somewhat overpredicted the measured attenuation of the turbulence however they were used during the design stage in order to decide what honeycombs, grids and contraction ratio to use. For a more recent paper concerning limitation of these formulae see Groth & Johansson (1988).

In the next section the results for a liquid jet with a turbulence intensity of $u'_L/\bar{u}_L = 0.8\%$ are presented. From now on this level of turbulence will be referred to as the smooth jet, since the liquid jet was visibly smooth. Later the results for a liquid jet with a turbulence intensity of $u'_L/\bar{u}_L = 3\%$ will be presented. This level of turbulence was found to produce a visibly rough jet.

EXPERIMENTAL RESULTS—SMOOTH JET

It was found that the best nozzle configuration to minimize the turbulence intensity of the jet at the nozzle exit was as follows:

(1) Two honeycombs separated by one half tube (inner) diameter, with the first honeycomb placed right after the nozzle inlet.
(2) Two grids separated one tube (inner) diameter apart. The first grid was a distance of one half tube (inner) diameter from the last honeycomb.

A high-speed Kodak (Spin Physics) videocamera with a zoom lens was used to visualize the induced two-phase flow. As shown schematically in figure 3, we observed that an annular meniscus was formed adjacent to where the jet impacted the liquid pool. Within this meniscus, a thin annular sheet of air was induced because of the drag of the liquid jet. This sheet of air became unstable leading to the entrainment of air bubbles. Figure 4(a) is a still picture extracted from the high-speed video. The meniscus can be seen in the bottom part of the near-field picture as well as the thin annular sheet of air. Near the bottom part of the picture waviness in the air sheet can be noted, however the air entrained process is not seen. Figure 4(b) shows a picture of the far-field process. The two-phase jet and the air entrained process can be observed. Near the surface, we did not observe bubbles, rather the air was present only in the thin annular sheet. This agrees with previous observations (Detsch & Sharma 1990) that breakup of the annular sheet of air causes air carryunder. The entrained bubbles were dispersed and a spreading two-phase jet eventually developed with the gas (i.e. dispersed) phase present in a conical configuration. We have also observed in the video that in the core of the liquid jet (i.e. near the centerline), the bubble number density was almost constant with time. In contrast, near the edge of the jet, we have observed sporadic bursts of bubbles, probably produced by the large liquid eddies of turbulent liquid, and the bubbles moved away from the centerline of the jet in the large eddies.

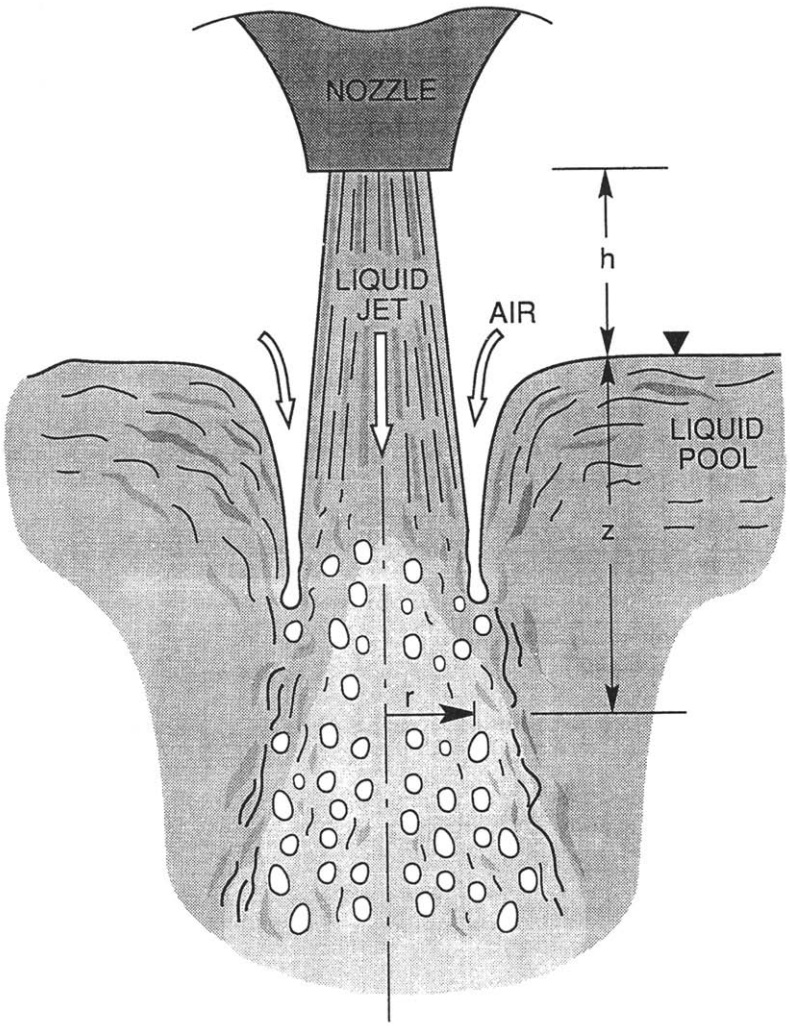

Figure 3. Schematic of the air entrainment process.

The FPDA system was focused on the centerline of the jet at a distance from the undisturbed free surface of the pool of $z = 35.1$ mm. The liquid jet's flow rate was $w = 0.143$ kg/s, and the distance from the nozzle exit to the surface of the liquid pool was $h = 9.0$ mm. Figure 5 shows the pdf for particle size. It can be seen that the distribution has a maximum for a bubble diameter of about 160 μm. Also, there is a pronounced peak for very low values of particle diameter. From this FPDA signal alone it was not possible to determine if the spike at the smallest diameter was produced only by liquid seeding. That is, the seeding of the liquid which was done using polystyrene particles having 9.5 μm mean diameter, as well as the particle inherent in the tap water which was used.

In order to better understand the origin of this peak, an experiment was run in which the liquid jet's mass flow rate was slightly lower than the threshold value for air entrainment. For this situation we measured only the liquid seeding signals, because there was no air entrainment. Next, we set the liquid flow rate through the nozzle to a value slightly exceeding the threshold for air entrainment. With this configuration we had approximately the same liquid seeding signals and we also had the signals produced by any small bubbles entrained. The histogram with only seeding particles had the same shape as the sharp peak at the lowest size shown in figure 5, however the data rate was approx. 10% of the data rate produced by the particles having diameters < 20 μm for the case in which air was being entrained. The conclusion is that the liquid seeding signals contribute to this peak but they do not account for all the small particles measured. In particular,

(a) Plunging liquid jet—near field

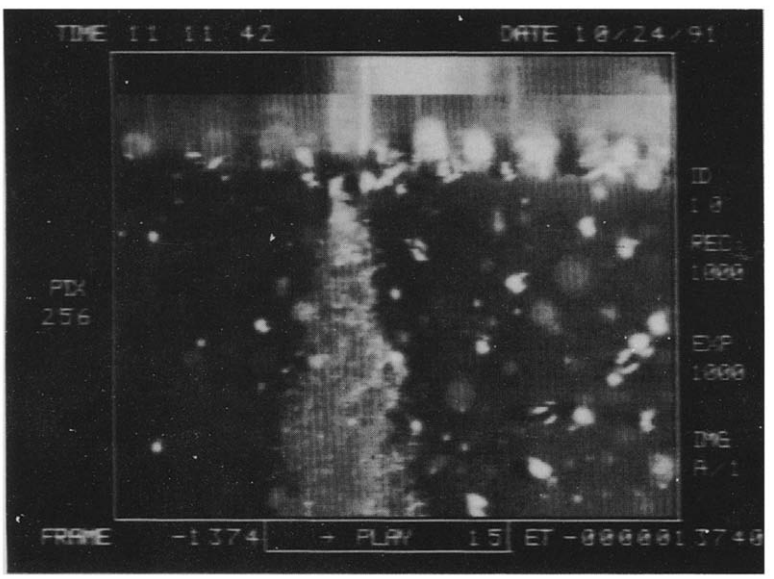

(b) Plunging liquid jet—far field

Figure 4. Photographs of the two-phase jet: (a) surface depression and the air film; (b) entrainment and dispersion of the air bubbles.

there was a significant number of air bubbles having a diameter $< 20\,\mu$m. These small bubbles are probably satellite bubbles that occur when the larger bubbles are split in the shear flow.

Figure 6 shows the pdf of the liquid phase velocity. The first-order moment of this distribution (i.e. the r.m.s. fluctuation) is defined as

$$u_L'^2 = \frac{1}{n-1}\sum_{i=1}^{n}(u_{Li} - \bar{u}_L)^2, \qquad [5]$$

The corresponding value of u_L' corresponding to figure 5 was 1.18 m/s. Interestingly, this is approximately equal to the u_L' corresponding to the single-phase flow value for the same position

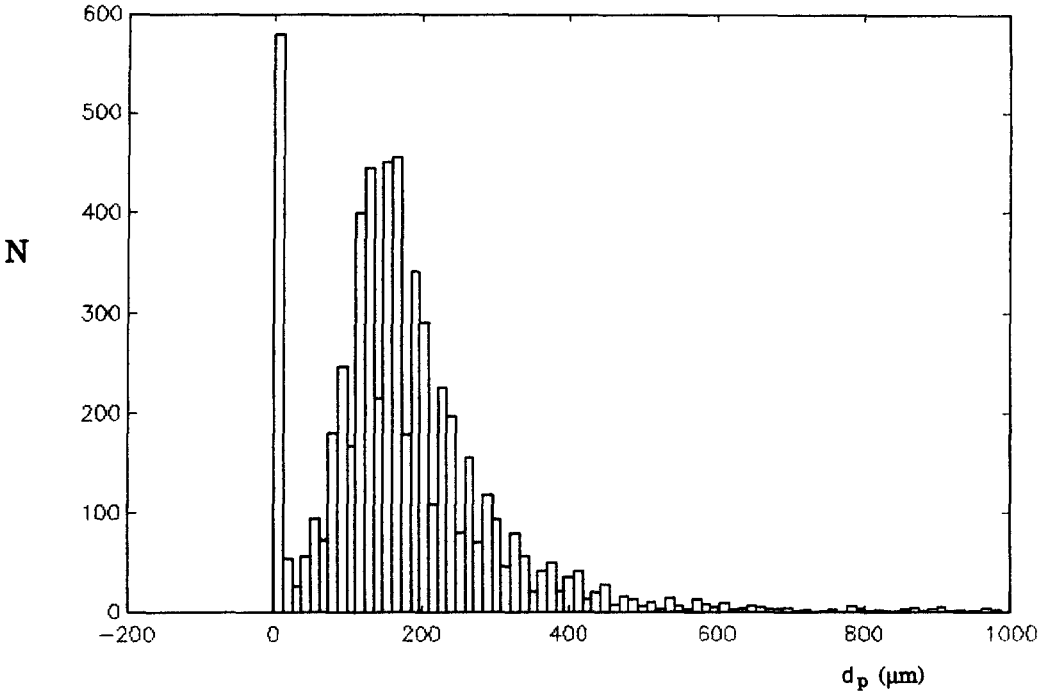

Figure 5. Particle diameter histogram—smooth jet ($z = 35.1$ mm; $w_L = 0.143$ kg/s; $h = 9.0$ mm, $r = 0$).

and liquid jet flow rate. This was characteristic of smooth jet behavior, and indicates that bubble-induced turbulence was very small compared to the shear-induced turbulence in the liquid phase.

The transit time (i.e. the residence time) of the particles in the measurement volume was also collected. A correlation between the transit time of a particle and its size and velocity was found. Moreover, it was found that using the information on the velocity and the transit time one could

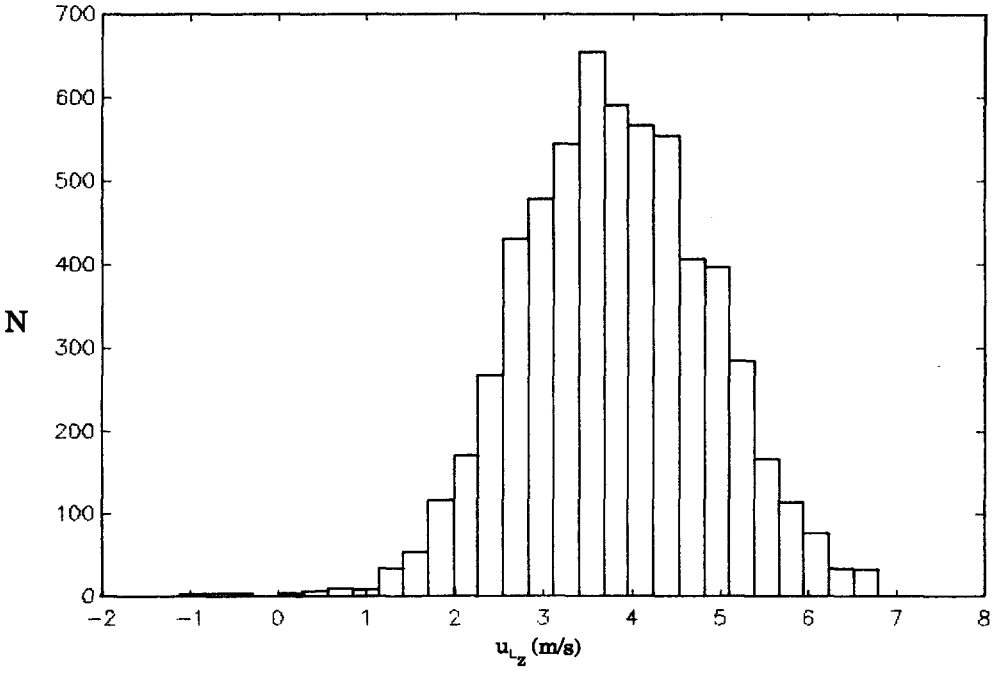

Figure 6. Liquid velocity ($d_p > 20\ \mu$m) histogram—smooth jet ($z = 35.1$ mm; $w_L = 0.143$ kg/s; $h = 9.0$ mm; $r = 0$).

predict if the bubbles have a size similar to the seeding particles or if they were larger. However, the velocity and transit time information alone was not enough to accurately calculate the bubble size. This fact can be easily understood if we suppose that the particles are much bigger than the measurement volume. Then the transit time is a function of the chord length of the particle and its velocity. In the best case the chord length can be calculated but this is not normally the bubble diameter. Thus, the transit time information could be used to sort between the liquid and gas velocities but could not be used for bubble size measurement.

The slip ratio (S) between the liquid and the gas was found to be near unity for the relatively small bubbles associated with a smooth liquid jet. It was actually somewhat lower than unity, because in two-phase jet downflow the gas velocity was lower than the liquid velocity due to buoyancy.

It was found that the bubbles with diameters $< 20\,\mu$m traveled at essentially the liquid phase velocity, while bubbles having diameters $> 20\,\mu$m were at a velocity which was somewhat less than the local liquid velocity.

Figure 7(a) depicts a contour plot of the two-dimensional pdf of the particle diameters (d_p) and axial bubble velocities (u_z). The plots are the curves of constant counts for the same conditions as in figures 5 and 6. Quantitatively the most probable value of peak 1 was at, $d_p = 5\,\mu$m, $u_z = 4.05$ m/s; and the most probable value of peak 2 was at $d_p = 125\,\mu$m, $u_z = 3.5$ m/s.

Figure 7(a) indicates that the velocity of the bubble was not dependent on its size. If the velocity of the bubbles had changed with size we would see the isocount curves with their principal axes forming an angle with the horizontal. There is no such trend observable in figure 7(a).

Figure 7(b) presents the same information as in figure 7(a) in a different way. For a given bubble diameter it shows the average axial bubble velocity u_z (the continuous line) and the r.m.s. fluctuation u_z' (i.e. the error bars). It can be clearly seen that the mean axial bubble velocity does not depend on the bubble diameter. Notice that figures 7(a) and 7(b) give for each bubble size the mean velocity, u_z, and the r.m.s. fluctuation, u_z', of the bubbles. This detailed information is necessary when one has particles of different diameters. In other words, an average velocity and an r.m.s. fluctuation is insufficient to compute the mass transfer characteristics accurately.

EXPERIMENTAL RESULTS—ROUGH JET

Figure 8 shows the liquid velocity histogram at the centerline of the liquid jet for a flow rate of $w = 0.144$ kg/s, a distance from the nozzle to the undisturbed pool surface of $h = 29.9$ mm and a distance from the pool surface to the measurement volume of $z = 33$ mm. The mean axial velocity is $u_L = 4.96$ m/s. One of the main differences between a rough liquid jet and a smooth jet is that in the latter case the liquid flow field is practically unaffected by the bubbles, while in the former the bubbles are much larger, thus the discrete phase increases the continuous phase's

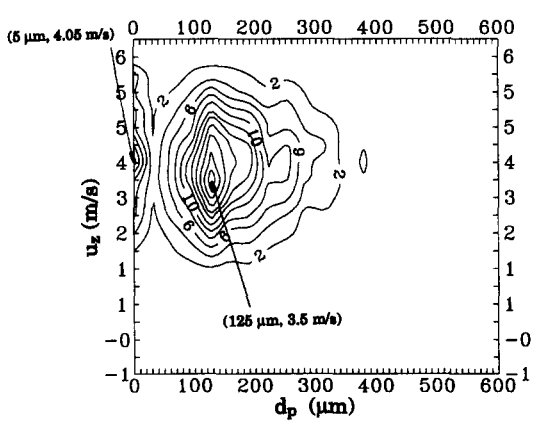

Figure 7(a). Contour plot of the two-dimensional pdf—smooth jet ($z = 35.1$ mm; $w_L = 0.143$ kg/s; $h = 9.0$ mm; $r = 0$).

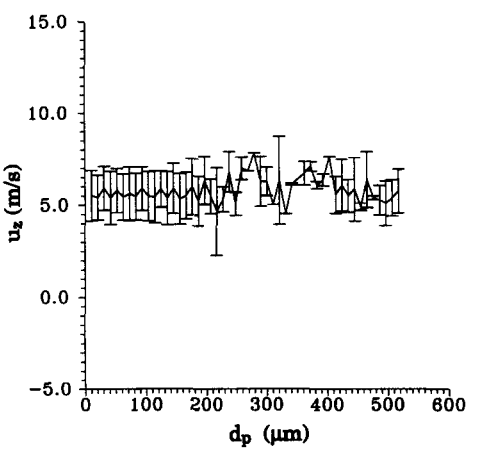

Figure 7(b). Mean velocity (continuous line) and r.m.s. fluctuation (error bars) as a function of the particle diameter—smooth jet ($z = 35.1$ mm; $w_L = 0.143$ kg/s; $h = 9.0$ mm; $r = 0$).

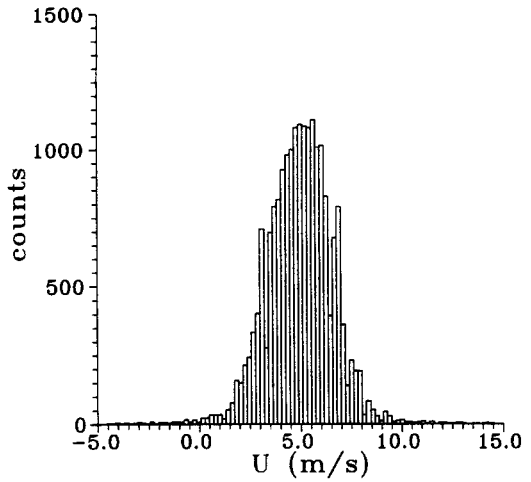

Figure 8. Liquid velocity histogram—rough jet ($z = 33$ mm; $w_L = 0.144$ kg/s; $h = 29.9$ mm; $r = 0$).

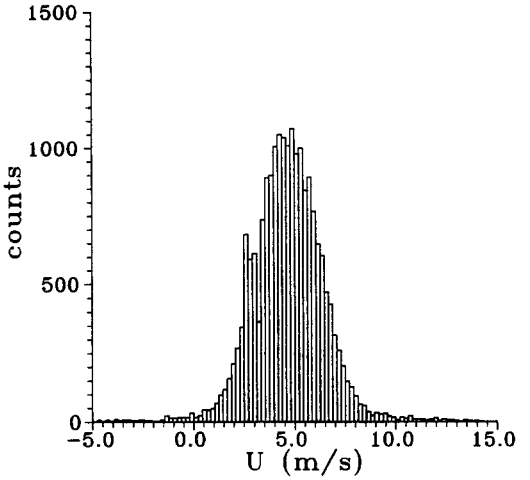

Figure 9. Gas velocity histogram—rough jet ($z = 33$ mm; $w_L = 0.144$ kg/s; $h = 29.9$ mm; $r = 0$.

turbulence intensity. This also increases phasic momentum exchange, resulting in greater dispersion of the two-phase jet and a lower velocity of the liquid velocity.

Figure 9 depicts the histogram of the gas velocity for the same conditions as figure 8. There is a significant difference between the mean values of the liquid velocity and the gas velocity, and this was generally true for the rough liquid jet data. The slip ratio in this case was < 1, and less than for the smooth jet due to the larger buoyancy associated with the bigger entrained bubbles.

Figure 10 presents the liquid and gas velocity as a function of radial position (r) for $h = 17.3$ mm, $w_L = 0.125$ kg/s and $z = 50.0$ mm. We see that at the edge of the spreading two-phase jet that the gas (bubble) velocity is negative, indicating buoyancy-driven countercurrent flow. It was also found that the two-phase jet was more dispersed than the corresponding single-phase flow case and that the turbulence intensity was higher. The turbulence enhancement is due to bubble-induced turbulence. In this case the bubble-induced turbulence accounts for about 30% of the total turbulence level.

Figure 11 shows for $w_L = 0.181$ kg/s, $h = 30$ mm, $z = 1$ mm and $r = 0$ (i.e. on the jet's centerline) the local void fraction, which is defined as the time fraction

$$\varepsilon = \sum_{i \in T} \frac{\Delta t_i}{T}. \qquad [6]$$

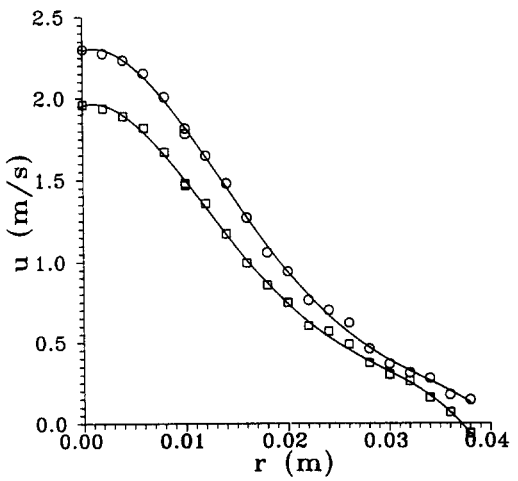

Figure 10. Liquid (○) and gas (□) mean velocities as a function of the radial distance—rough jet ($z = 50.0$ mm; $w_L = 0.125$ kg/s; $h = 17.3$ mm).

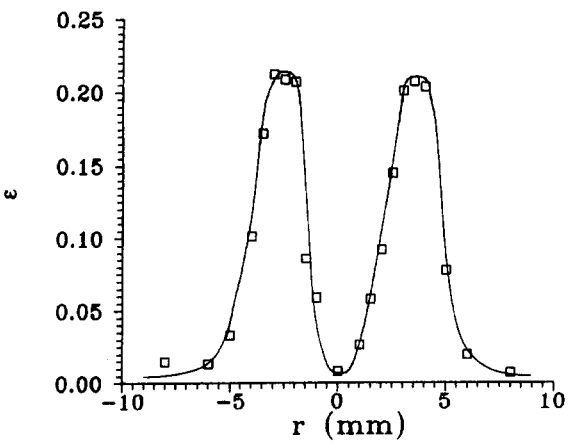

Figure 11. Void fraction as a function of the distance from the centerline—rough jet ($w_L = 0.181$ kg/s; $h = 30$ mm; $z = 1$ mm).

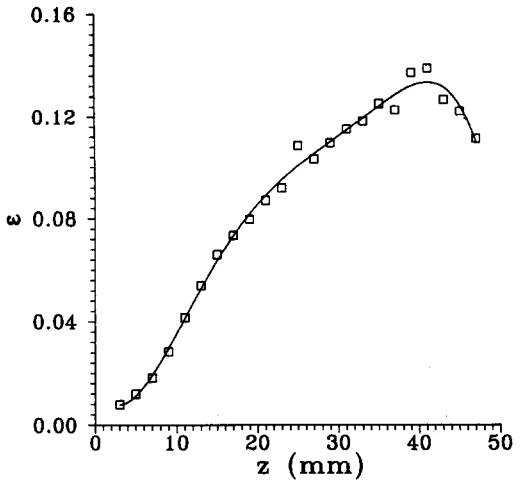

Figure 12. Void fraction as a function of the distance beneath the undisturbed pool level—rough jet ($w_L = 0.181$ kg/s; $h = 30$ mm; $r = 0$).

As discussed previously, a KfK impedance probe was used for these void fraction measurements. A post-processing of the properly thresholded signals was used to evaluate the local void fraction. The axial location $z = 0$ in figure 12 corresponds to the point of impact of the liquid jet if the pool surface was undisturbed under the centerline of the liquid jet (i.e. at $r = 0$). The value of the local void fraction at this point was zero because only liquid was present. As the measurement volume was moved down (i.e. $z > 0$) bubble carryunder and dispersion occurs which causes the local void fraction at $r = 0$ to increase with z. A competing mechanism that causes the void fraction to later decrease is that the two-jet spreads as we increase z. In the case shown the maximum void fraction on the jet's centerline ($r = 0$) is at about $z = 42$ mm.

DATA QUALIFICATION

In order to test our measurement system as well as the symmetry of the data, the void fraction profiles were measured through the two-phase jet for various axial positions (z). In figure 11 the void fraction data at $z = 1$ mm is shown. The positive r readings correspond to one side of the jet while the negative r values to the other side. We note that the void fraction was symmetric within the experimental error ($\Delta\epsilon = \pm 0.01$).

After each refill of the test loop with fresh water, and before discharging the used water, a void fraction and velocity profile were measured for conditions which were established as a benchmark. Excellent reproducibility was observed, which indicates that the effect of any surface tension variation due to water impurity was not strong.

As noted previously, when the liquid jet impacts the pool surface, air entrainment occurs around the jet's circumference. In figure 13(a) the measured local void fraction is presented as a function of r for $z = 1$ mm (i.e. with the probe 1 mm under the undisturbed liquid level). We see that the void fraction has a maximum at $r \cong d_{jet}/2 \cong 2.5$ mm. Obviously, the air entrainment process is responsible for this effect. In the high-speed video visualization of these experiments it was rare to observe bubbles at the liquid jet's centerline for $z < 10$ mm. However, once the air was entrained, dispersion of the gas phase occurred as z was increased. Figure 13(b) shows how the void peaks in figure 13(a) were dispersed at $z = 18$ mm. We see that the maximum now occurs at $r \simeq 5$ mm. Moreover, we see that there is a significant void fraction at $r = 0$ (i.e. the jet's centerline) because of the void dispersion process. Figure 13(c) shows the void fraction profile at $z = 43$ mm. Significantly, the curve now has a maximum at the centerline of the jet ($r = 0$). Again, this is a direct result of the void dispersion process in the two-phase jet.

This information is summarized in figure 14, where it can also be easily observed how the two-phase flow jet disperses as z increases. Finally, figure 15 shows that the amount of air entrained is a strong function of the distance, h, of the nozzle exit above the undisturbed pool surface. With

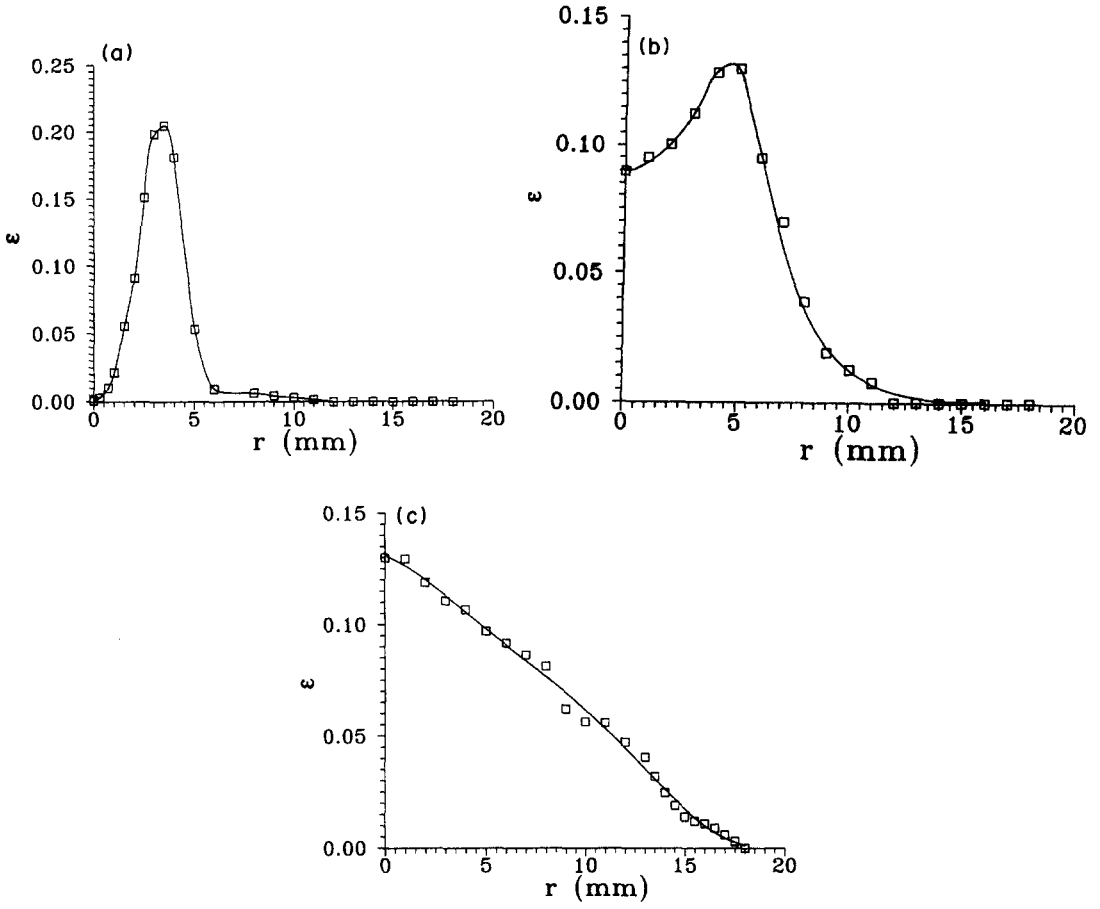

Figure 13. Void fraction as a function of the distance from the centerline—rough jet ($w_L = 0.181$ kg/s; $h = 30$ mm): (a) $z = 1$ mm; (b) $z = 18$ mm; (c) $z = 43$ mm.

everything else held constant, the void fraction increased with h because the larger the h, the larger the roughness of the jet when it impacts the liquid pool.

Interestingly, off-centerline peaking of the void fraction was not reported by McKeogh & Ervine (1981) for similar conditions (i.e. $u_L'/\bar{u}_L = 5\%$, $d_{jet} = 9$ mm, $w_L = 0.199$ kg/s). This is presumably because the data presented herein is based on more detailed local measurements.

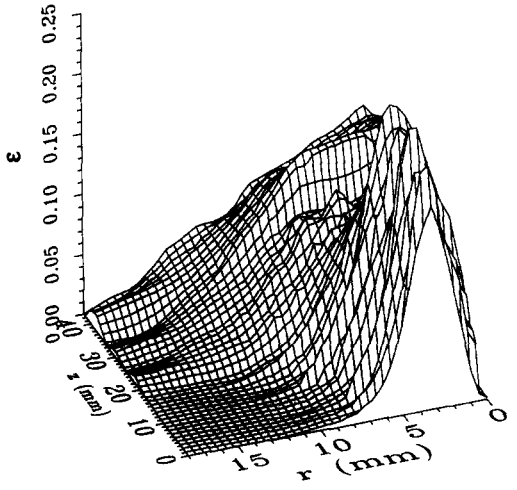

Figure 14. Void fraction as a function of r and z—rough jet ($w_L = 0.181$ kg/s; $h = 30$ mm).

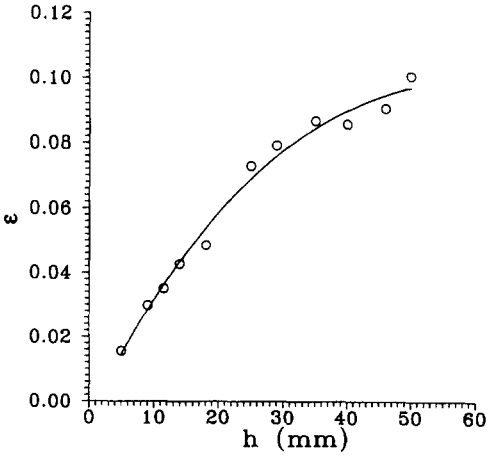

Figure 15. Void fraction as a function of the distance from the nozzle exit to the undisturbed water level—rough jet ($w_L = 0.127$ kg/s; $h = 30$ mm; $z = 35$ mm; $r = 0$).

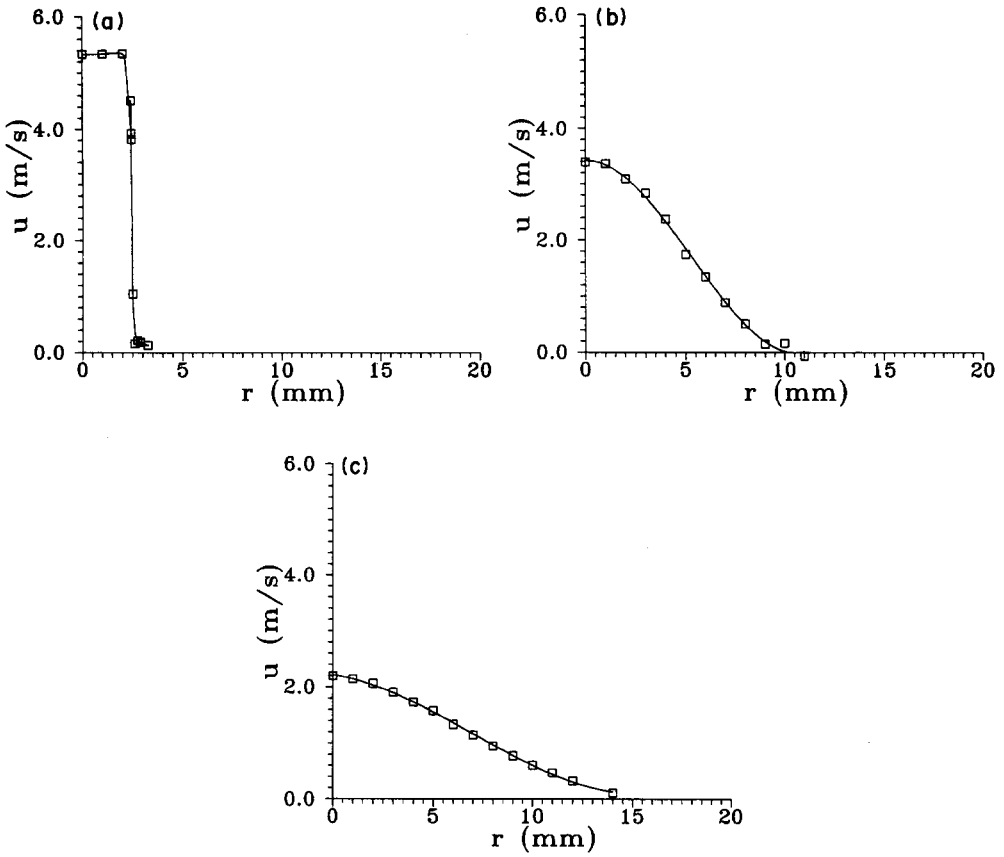

Figure 16. Liquid velocity as a function of distance from the centerline—rough jet ($w_L = 0.107$ kg/s): (a) $h = -30$ mm, $z = 0.1$ mm; (b) $h = 10$ mm, $z = 18$ mm; (c) $h = 10$ mm, $z = 43$ mm.

Figures 16(a–c) present the mean liquid velocity (u_L) as a function of the radial distance r for three different distances (z) from the undisturbed pool level. Figure 16(a) is a measurement of the liquid velocity profile at the exit of the nozzle. This flat profile is characteristic of the potential flow which exited from the nozzle.

Figures 16(b) and (c) show that the liquid velocity curves have a maximum at the centerline for all z. Comparing these two profiles one can see how the two-phase jet spreads.

SUMMARY AND CONCLUSIONS

Detailed measurements were taken of the three-dimensional void fraction and liquid velocity fields beneath a plunging liquid jet. In particular, detailed new LDA/FPDA data have been taken of the air carryunder process associated with a plunging cylindrical liquid jet. The size distribution of the entrained air bubbles has been measured directly with the FPDA system. It was found that for a smooth jet the entrained bubbles were very small ($\bar{d}_b \cong 120\ \mu$m). For this case the slip ratio was nearly unity, and the turbulent intensity of the liquid phase was comparable to single-phase liquid jets.

The FPDA system was found to be especially well-suited for small bubble size measurements in two-phase jets. With our particular setup we could measure bubble diameters up to about 1 mm. We did not use the FPDA to measure the bubble diameters with the rough jet.

In contrast, for a turbulent (i.e. rough) liquid jet the entrained bubble sizes were of the order of $d \cong 2$ mm, and the slip ratio was close to calculated values based on the terminal rise velocity of a single bubble. Moreover, the turbulence intensity of the liquid jet had two components, one due to shear-induced turbulence and the other due to bubble-induced pseudo-turbulence. Both components of turbulence were of the same order of magnitude.

The FPDA system was found to be especially well-suited for small bubble size measurements in two-phase jet flows.

These data provide the insight necessary for the development of analytical models of the air entrainment process. Moreover, they should also be useful for benchmarking phenomenological or mechanistic computational fluid dynamic (CFD) analysis of the dispersion process in the induced two-phase jet.

Acknowledgements—The financial support of this study by the Office of Naval Research (ONR) Grant No. N-0001491-J-1271 of the ONR Fluid Dynamics Program-1132F is gratefully acknowledged. In addition, the assistance of Professors H. Nagamatsu (RPI) and A. Hirsa (RPI) in the design of this experiment was very helpful and is much appreciated.

REFERENCES

AVERY, S. & NOVAK, P. 1978 Oxygen transfer at hydraulic structures. *J. Hydraul. Div. ASCE* **104,** 1521–1540.

BLANCHARD, D. & CIPRIANO, R. 1981 Bubble and aerosol spectra produced by a laboratory breaking wave. *J. Geophys. Res.* **86c,** 8085–8092.

BURGESS, J. M., MOLLOY, N. A. & MCCARTHY, M. J. 1972 A note on the plunging liquid jet reactor. *Chem. Engng Sci.* **12,** 442–445.

DETSCH, R. & SHARMA, R. N. 1990 The critical angle for gas bubble entrainment by plunging liquid jets. *Chem. Engng Sci.* **44,** 157–166.

DRYDEN, H. L. & SCHUABAUEN, G. 1947 The use of damping screens for the reduction of wind tunnel turbulence. *J. Aerosol Sci.* **14,** 221–228.

DURST, F. & ELIASSON, B. 1975 Properties of laser Doppler signals and their exploitation for particle size measurements. In *Proc. LDA Symp.*, Copenhagen, pp. 115–137.

ERVINE, D. A. & FALVEY, H. 1987 Behavior of turbulent water jets in the atmosphere and in plunging pools. *Proc. Inst. Civ. Engrs* **83,** 295–314.

ERVINE, D. A., MCKEOGH, F. & ELSAWAY, E. 1980 Effect of turbulence intensity on the rate of entrainment by plunging water jets. *Proc. Inst. Civ. Engrs* **69,** 425–445.

GROTH, J. & JOHANSSON, A. 1988 Turbulence reduction by screens. *J. Fluid Mech.* **197,** 139–159.

HEWITT, G. B. 1978 *Measurement of Two-phase Parameters.* Academic Press, London.

KERMAN, B. R. 1984 A model of interfacial gas transfer for a well-roughened sea. *J. Geophys. Res.* **89**(D1), 1439–1446.

KOGA, M. 1982 Bubble entrainment in breaking wind waves. *Tellus* **34,** 481–489.

LIN, T. J. & DONNELLY, H. G. 1966 Gas bubble entrainment by plunging laminar liquid jets. *AIChE Jl* **12,** 563–571.

MCKEOGH, E. J. & ELSAWAY, E. 1980 Air retained in pool by plunging water jet. *J. Div. ASCE* **106,** 1577–1593.

KCKEOGH, E. J. & ERVINE, D. A. 1981 Air entrainment rate and diffusion pattern of plunging liquid jets. *Chem. Engng Sci.* **36,** 1161–1172.

MIE, G. 1908 Beiträge zur Optik trüber Medien, Speziell Kolloider Metallösungen. *Annln Phys. (Leipzig)* **25,** 377–445.

MONAHAN, L. & TORGERSEN, T. 1991 In *Air–Water Mass Transfer* (Edited by WILHELMS, S. & GULLIVER, J.). ASCE, New York.

MORAL, T. 1977 Design of two-dimensional wind tunnel contractions. *J. Fluids Engng* **61,** 371–378.

OHKAWA, A., KUSABINSKI, D., KAWAI, Y., SAKAI, N. & ENDOH, K. 1986 Some flow characteristics of a vertical liquid jet system having downcomers. *Chem. Engng Sci.* **51,** 2347–2361.

PRANDTL, L. 1933 Attaining a steady air stream in wind tunnels. Report NACA TM 726.

RAE, W. & POPE, A. 1984 *Low Speed Wind Tunnel Testing*, 2nd edn. Wiley-Interscience, New York.

SAFFMAN, M., BUCHHAVE, P. & TANGER, A. 1984 Simultaneous measurement of size, concentration and velocity of spherical particles by a laser Doppler method. Paper presented at the *2nd Int. Symp. on Applications of Laser Anemometry to Fluid Mechanics*, Lisbon, Portugal.

SCHEIMAN, J. & BROOKS, J. D. 1981 Comparison of experimental and theoretical turbulence reduction from screens, honeycombs, and honeycomb–Screen combinations. *J. Aerosol Sci.* **18,** 638–643.

SENE, K. 1988 Air entrainment by plunging jets. *Chem. Engng Sci.* **43,** 2615–2623.

VAN DE SANDE, E. & SMITH, J. M. 1973 Surface entrainment of air by high velocity water jets. *Chem. Engng Sci.* **28,** 1161–1168.